Electron Impact on Atmospheric Gases 3. Spatial Yield Spectra for N_2

C. H. JACKMAN AND A. E. S. GREEN

University of Florida, Gainesville, Florida 32611

Spatial yield spectra have been calculated for electron energy degradation into molecular nitrogen gas using a Monte Carlo method for 0.1- to 5.0-keV incident electrons. These spectra contain the spatial yield information about the electron degradation process and can be employed to calculate a 'yield' for any inelastic state at any position in the medium. Because of the spectrum's useful nature and simple characteristics, the three-variable spatial yield spectrum $U(E, z, E_0)$ is analytically represented as well. This analytic form can then be easily applied to atmospheric and laboratory problems dealing with energetic electron degradation.

1. INTRODUCTION

The first two papers of this series were concerned with the nonspatial aspects of electron impact on atmospheric gases. The first paper, by *Jackman et al.*, [1977], updated the cross sections of six atmospheric gases (namely, N_2, O_2, O, CO, CO_2, and He). The second paper, by *Green et al.* [1977], then used the cross sections for these gases along with the cross sections for Ar, H_2, and H_2O in a modified discrete energy bin method of electron energy degradation. A 'yield spectrum' was introduced in that paper which is amenable to physical interpretation, accurate analytic representation, and convenient application for the determination of many yields needed in aeronomical problems.

This yield spectrum, while accurate for calculating the total yield of any state, does not provide information about the spatial distribution of the yield. As experimental probings of the atmosphere become more accurate, the need for spatial knowledge of the yield becomes more acute. Molecular nitrogen is studied here in an attempt to generalize some of the characteristics of the spatial electron energy deposition problem.

Several spatial electron energy deposition approaches exist. These include the Fokker-Planck method of *Walt et al.* [1967], the hybrid approach (involving the Fokker-Planck equation for electron energies above 500 eV and the two-stream method for electron energies below 500 eV) of *Banks et al.* [1974], the Monte Carlo approach of *Berger et al.* [1970, 1974], the Monte Carlo approach of *Cicerone and Bowhill* [1970, 1971], and the multiangle equation of transfer solution of *Strickland et al.* [1976]. *Mantas* [1975] and *Jasperse* [1976, 1977] also use spatial electron energy deposition techniques to solve the equation of transfer but concentrate their efforts on photoelectrons.

A Monte Carlo energy deposition technique is applied in this study to electrons with incident energies from 0.1 to 5.0 keV. The incident electrons and their secondaries and tertiaries are followed in a collision-by-collision manner down to 30 eV. Below 30 eV a multiple elastic scattering distribution is used down to the cutoff energy of 2 eV.

2. CROSS SECTIONS

a. *Elastic Cross Sections*

The elastic collisions cause the most scattering of electrons; thus special care must be taken in regard to the elastic differential cross sections. In this study two different forms of the differential elastic cross section will be described and then contrasted when used in the Monte Carlo approach to electron energy deposition.

The first form, the screened Rutherford cross section, is expressed as

$$P_{SR}(\theta, E) = \frac{Z^2 e^4}{p^2 v^2 (1 - \cos\theta + 2\eta)^2 \sigma_R(E)} \tag{1}$$

in phase function form, where Z is the atomic number of the substance, e is the electronic charge, p is the momentum of the electron, v is the velocity of the electron, θ is the polar scattering angle,

$$\sigma_R(E) = \frac{Z^2 51.8\pi}{E^2 \eta(1 + \eta)} \quad \text{Å}^2\,\text{eV}^2 \tag{2}$$

$$\eta = \eta_c \frac{1.70 \times 10^{-5} Z^{2/3}}{\tau(\tau + 2)} \tag{3}$$

[*Moliere*, 1947, 1948], $\tau = E/mc^2$ is the electron energy in units of the electron rest energy, and η_c is assumed to be 1.0 (following the work of *Berger et al.* [1970]). In the energy regime of interest ($E \leq 5$ keV), $\tau \ll 2$, $Z = 7$, and, consequently, $\eta \approx 16/E$.

This form, Equation (1) (hereafter called SR), while used reasonably successfully by *Berger et al.* [1970, 1974], tends to underestimate the sharply forward peaked small-angle scattering, overestimate the medium-angle scattering, and underestimate the large-angle scattering.

Ivanov et al. [1977] have recently attempted to describe the differential elastic cross sections of N_2, O_2, and O using a form which includes a sharper forward scattering component along with a backward scattering peak. *Porter and Jump* [1978] then pointed out some of the deficiencies in this representation and have employed a more convenient form to represent the elastic differential cross sections of N_2, O_2, O, CO, CO_2, and He. They fitted experimental data fairly well, but only at several separate energies for each gas. Thus use of their differential cross section form in a deposition calculation probably would require the use of spline functions or other interpolative techniques.

In this paper an energy-dependent representation was desired which also included the near-exponentiallike fall-off (pointed out by *Shyn et al.* [1972] and *Herrmann et al.* [1976]) at the small angles and the backscattering peak at the large angles which is observed for electron energies less than 200 eV. The phase function form chosen is normalized to one with an integration over the solid angle and is represented as (hereafter

Paper number 9A0208.
0148-0227/79/009A-0208$01.00

TABLE 1. Parameters Used in (4)

Parameter	Value	Parameter	Value
f_{11}	100 eV	a	0.11
f_{12}	0.84	b_1	0.43
f_{13}	1.92	b_2	−0.29
f_{21}	10 eV	c_1	1.27
f_{22}	0.51	c_2	12 eV
f_{23}	0.87	c_3	0.27

$f_1(E) = (E/f_{11})^{f_{12}}/[(E/f_{11})^{f_{12}} + f_{13}]$
$f_2'(E) = (E/f_{21})^{f_{22}}/[(E/f_{21})^{f_{22}} + f_{23}]$
$f_2(E) = 1 - f_1(E)$, for $E > 200$ eV
$f_2(E) = f_2'(E)\,[1 - f_1(E)]$, for $E \leq 200$ eV
$b(E) = b_1 \left(\frac{E}{1\text{ eV}}\right)^{b_2}$
$c(E) = c_1\left[1 - \left(\frac{c_2}{E}\right)^{c_3}\right]$

called EX)

$$P_{EX}(\theta, E) = \frac{f_1(E)[1 - b^2(E)]e^{-\theta/b(E)}}{2\pi b^2(E)[1 + e^{-\pi/b(E)}]} - \frac{f_2(E)}{2\pi[(2 + a)^{-1} - a^{-1}][1 - \cos\theta + a]^2} - \frac{[1 - f_1(E) - f_2(E)]}{2\pi[(2 + c(E))^{-1} - c(E)^{-1}][1 + \cos\theta + c(E)]^2} \quad (4)$$

The parameter expressions for (4) are given in Table 1.

Comparison of these two forms, SR and EX, with the experimental data is given in Figures 1*a* and 1*b* at the two energies of 30 eV and 1000 eV. The EX form given by (4) fits the data quite well at these two representative energies and at the other energies as well.

Both of these forms are normalized to the same total elastic cross section given by

$$\sigma(E) = T\left\{\frac{E^X}{\eta(\eta + 1)[V^{2+X} + E^{2+X}]} + \frac{F_1G_1^2}{(E - E_1)^2 + G_1^2} + \frac{F_2G_2^2}{(E - E_2)^2 + G_2^2}\right\} \quad (5)$$

Here, $\eta = U/E$, and the other parameter values for N_2 are presented in Table 2. *Porter and Jump* [1978] presented this form which falls off as $1/E$ in the large-energy limit (similar to the screened Rutherford cross section given in (2)) and which contains two other terms (the second and third terms) that describe the low-energy shape and Feshbach resonances. This form is presented in Figure 2 as the dashed line.

b. Inelastic Cross Sections

The total inelastic cross sections for N_2 were all taken from *Jackman et al.* [1977] and *Porter et al.* [1976]. The differential inelastic cross sections were dealt with in the following manner: (1) The scattering of the primary electron in an ionization event was described using the form given in *Porter et al.* [1976]; (2) the scattering of the secondary electron in an ionization event is described using (6); and (3) the scattering phase function for the electron as a result of the inelastic excitation event was considered only at incident electron energies below 100 eV. In this energy regime the inelastic scattering was calculated with the use of the elastic phase function.

First, consider the differential ionization cross sections. The triply differential ionization cross section $d\sigma/dT\,d\Omega_{sec}\,d\Omega_{Prim}$ (where T is the secondary energy, Ω_{sec} is the secondary scattering angle, and Ω_{Prim} is the primary scattering angle) of an electron of incident energy E has only recently been measured. There is a connection between the primary electron and the secondary electron scattering after an ionization event; however, for N_2 this interaction was measured only at one energy, $E = 100$ eV [see *Jung et al.*, 1975]. Very few experimental and theoretical triply differential cross-section data exist with which to work, and thus we focus in this paper on the doubly differential ionization cross section.

The primary doubly differential cross section form is taken from *Porter et al.* [1976, Equation (14)], while the secondary doubly differential cross section form is given below. The most extensive work on these secondary cross sections is that of

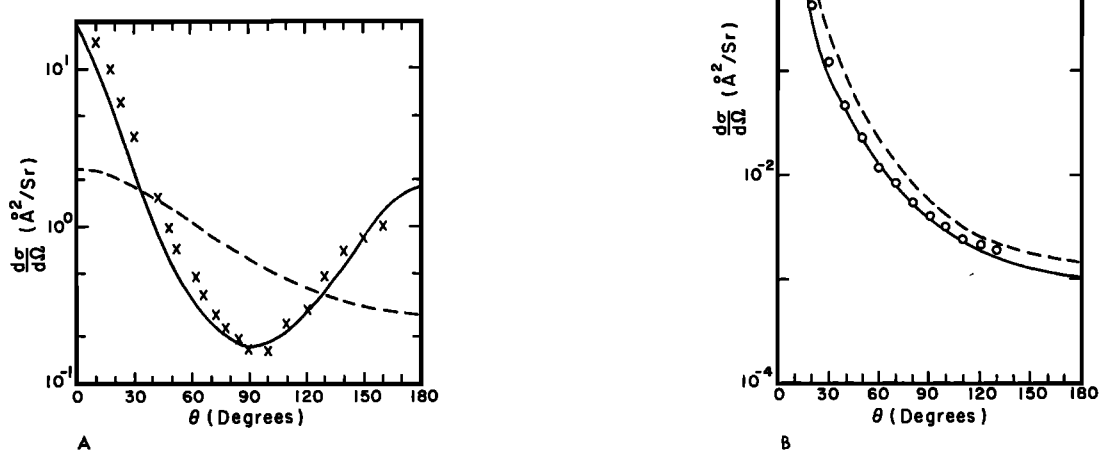

Fig. 1. N_2 electron impact elastic differential cross sections. The SR (dashed line) and the EX (solid line) forms are compared with the experimental data of *Shyn et al.* [1972] (crosses) and *Herrmann et al.* [1976] (circles) at the energies of (*a*) 30 eV and (*b*) 1000 eV.

Opal et al. [1972]. These data indicate a preferred angle of scattering (usually between 45° and 90°) at all incident and secondary electron energies; thus a Breit-Wigner form has been chosen to represent the data. Here,

$$\frac{d\sigma}{dTd\Omega} = \frac{S(E, T)C^2}{[C^2 + B(\cos\theta - \cos\theta_0)^2]Nf} \quad (6)$$

$$S(E, T) = \frac{d\sigma}{dT} = \frac{A(E)\Gamma^2(E)}{[(T - T_0(E))^2 + \Gamma^2(E)]} \quad (7)$$

is from *Green and Sawada* [1972], the parameter expressions for both (6) and (7) being given in Appendix 1. Equation (6) is defined so that integration over the solid angle is given very simply as (7).

Two papers, by *Cartwright et al.* [1977] and *Chutjian et al.* [1977], have recently been published which present inelastic differential cross sections for several low-lying excitation states of N_2 at a few incident electron energies between 10 eV and 60 eV. These data suggest that these inelastic collisions cause approximately the same amount of scatter as that resulting from elastic collisions at electron energies between 10 eV and 60 eV. Therefore it is assumed in this work that the pitch angle distributions are the same for both the inelastic and the elastic events at electron energies below 100 eV.

Above 100 eV the optically allowed excitations are the most important inelastic excitation events. Since these excitation processes exhibit very highly peaked forward scattering at the higher electron energies, it is assumed that inelastic excitations will not change the direction of the incident electron whose energy is above 100 eV.

The cross sections for the inelastic states given in *Jackman et al.* [1977] were summed and are presented in Figure 2. Above 30 eV the cross section was fit with the function (for convenient use)

$$\sigma_{TI}(E) = \frac{q_0 F[1 - (W/E)^\alpha]^\beta \ln((4EC/W) + e)}{WE} \quad (8)$$

where $q_0 = 651.3$ Å^2 eV^2 and e is the natural logarithm base, equal to 2.71828. This form has the characteristic Born-Bethe $E^{-1} \ln E$ fall-off behavior at the large energies. The parameters $\alpha = 1$, $\beta = 4.81$, $C = 0.36$, $F = 4.52$, and $W = 11$ eV were found with the use of a nonlinear least square fitting program which fit (8) to the sum of all the inelastic cross sections. From 30 eV up to 5 keV this form was used for the total inelastic cross section. Below 30 eV the total inelastic cross section was read in numerically for use in the electron energy deposition scheme.

The total cross section which is a sum of the inelastic and the elastic cross sections is given in Figure 2 as the dash-dot line and is compared with the experimental data of *Blaauw et al.* [1977]. Throughout the energy range the cross sections used in this study compare favorably with these experimental values.

3. Monte Carlo Electron Degradation Technique

A Monte Carlo calculation is used in this work for energy degradation by energetic electrons in N_2. This stochastic process can be the most accurate method for obtaining the energy loss of particles in a medium if sufficient computer time is available. Basically, each electron is degraded in a collision-by-collision manner from the incident electron energy down to 2 eV.

In this Monte Carlo calculation the electrons were monoenergetic, monodirectional, and incident along the z axis in a bounded medium (the bounds on the medium were chosen large enough that for most practical purposes it is an infinite medium). The sample sizes ranged from 2000 electrons at energies 100 and 300 eV to 200 electrons at 5000 eV. 1000 electrons were used at 1000 eV and 500 electrons were used at 2000 eV. Through the use of these sample sizes the statistics stayed about the same in all the comparisons.

TABLE 2. Parameters Used in (5)

Parameter	Value	Parameter	Value
$\bar{T}$	2.5×10^{-6} cm^2	F_1	7.33
U	1.95×10^{-3} eV	E_1	2.47 eV
V	150 eV	G_2	24.3 eV
X	−0.770	F_2	2.71
G_1	0.544 eV	E_2	15.5 eV

The cross sections used in these Monte Carlo calculations are taken from section 2. The path length between collisions was calculated using (3) from *Heaps and Green* [1974].

The scattering event is recorded as either an elastic or an inelastic collision. In the elastic collision, the scattering angle calculation is the next concern. If the scattering event is inelastic, then the state that is excited must be calculated.

For the purposes of expediency and reducing the cost of the Monte Carlo calculation, the number of states in N_2 was reduced from thirty-four states down to nine states. Two allowed states, the $b\ ^1\pi_u$ and the $b'\ ^1\Sigma_u^+$, and the six ionization states were kept the same as given in the *Jackman et al.* [1977] paper. For the ninth state, all the Rydberg and forbidden states were combined. Use of this simplification in the Monte Carlo calculation gave no apparent change in the resultant yield spectra or intensity plots.

The polar scattering angle of the electron was then calculated after the type of collision had been established. An analytic function was used for the SR phase function and the secondary electron scattering because (1) and (6) are easily inverted to give the polar angle as a function of the random number. For the EX phase function the angular range from 0° to 180° was divided into 24 intervals, and the polar scattering angle was then calculated by linear interpolation after placing the random number in its proper interval. The azimuthal scattering angle was assumed to be isotropic for all scattering

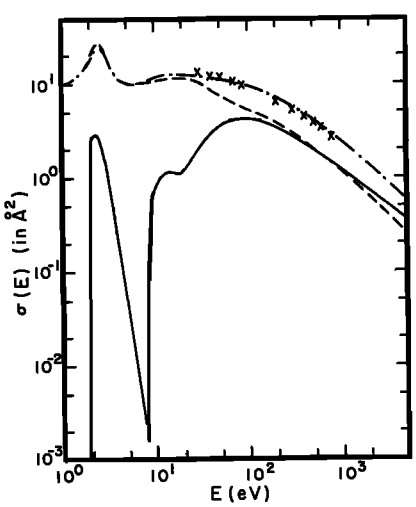

Fig. 2. N_2 electron impact cross sections. The total inelastic (solid line); total elastic (Equation (5), dashed line); total inelastic plus elastic (dash-dot line); and the experimental inelastic plus elastic values [*Blaauw et al.*, 1977] (crosses) are presented here.

events. Many of the details of calculating the angles of scatter are pointed out by *Berger et al.* [1970] and *Heaps and Green* [1974].

A collision-by-collision degradation scheme was used down to 30 eV. At this energy, the elastic collisions are occurring with twice the frequency of the inelastic events, and at energies below 30 eV the number of elastic collisions between inelastic events may be up to several hundred or a thousand. Keeping track of all these elastic collisions would be very costly. We thus use a multiple elastic scattering distribution to characterize the electron's coordinates at each inelastic collision.

Kutcher and Green [1976] studied the radial, longitudinal, and polar angle distributions for elastic scattering by H_2 in the energy range from 2 to 50 eV. Rather than repeat such a project for N_2 which would require a substantial amount of computer time and money, the possibility of using the H_2 multiple elastic scattering distribution results was considered.

The differential elastic cross sections for N_2 and those used for H_2 in the work by *Kutcher and Green* [1976] are slightly different. There is more backscatter observed experimentally in N_2 at all energies. We assume in this paper that the longitudinal coordinate is the only one affected by this difference. (In this work the longitudinal coordinate is that coordinate measured parallel to the incident direction of the electron and the radial coordinate is that coordinate measured perpendicular to the longitudinal coordinate.)

For reasons given by *Jackman* [1978], the longitudinal distance z (in units of mean free path lengths (hereafter called MFPs)) can be written as

$$z = \ln\left(\frac{\{[R^{-1/\nu} - 1]/[F(O)^{-1/\nu} - 1]\}}{-u}\right) \tag{9}$$

where R is a random number and the rest of the parameters are given in Table 3.

The expression for ρ, found by inverting (8) of *Kutcher and Green* [1976], is written

$$\rho = [-\ln(1 - R)/\delta]^{1/\gamma} \tag{10}$$

where

$$\delta = (22 + (s/0.3)^{1/2})/(s + 0.3)^{1.5} \tag{11}$$

$$\gamma = 2[1 - \exp(-s/4)] \tag{12}$$

and R is a random number. The parameters are found by averaging those parameters in Table 1 of *Kutcher and Green* [1976].

Above five or six MFPs the polar angle is approximately random. At most energies below 30 eV, the number of MFPs between inelastic collisions is above five or six. Since the distribution found in *Kutcher and Green* [1976] is not easily inverted, a reasonable assumption is that the polar angle is oriented randomly.

TABLE 3. Parameters From *Kutcher and Green* [1976] for Several Energy Intervals Used in (9)

Energy Interval, eV	H	I	J	D	s_ν	s_F
2–5	12.	1.37	1.71	1.75	5.05	8.5
5–10	9.6	1.32	1.67	2.50	4.25	8.5
10–20	15.5	1.28	1.67	2.31	6.29	10.3
20–30	23.5	1.24	1.69	1.98	9.65	13.6

$\nu(s) = 1 - \exp[-(s/s_\nu)^D]$
$F(O) = K\{1 - \exp[-(s/s_f)^{0.75}]\}$
$u(s) = (H + s^I)/s^J$
The s is the path length to the inelastic collision (defined in (13)). Following *Jackman* [1978], we set $K = 0.46$.

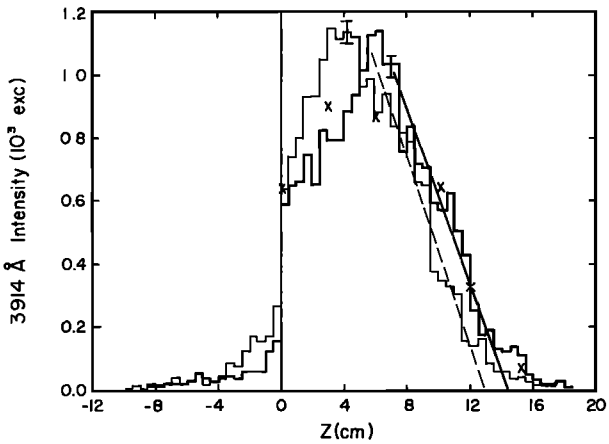

Fig. 3. Intensity plot for electrons of energy 2 keV is presented as a function of the longitudinal direction. The crosses represent relative experimental values from *Barrett and Hays* [1976], and the histograms present the data which result from use of the EX (heavy line) and the SR (light line) elastic phase functions in a Monte Carlo calculation. The straight solid and the straight dashed lines represent extrapolations to find the ranges for these two elastic differential cross section models.

The total path length s, used in (9)–(12), is calculated from a random number R, the total elastic cross section $\sigma_{TE}(E)$, and the total inelastic cross section $\sigma_{TI}(E)$, by using

$$s = -\frac{\sigma_{TE}(E)}{\sigma_{TI}(E)} \ln(R) \tag{13}$$

The ratio $\sigma_{TE}(E)/\sigma_{TI}(E)$ is simply a fairly accurate approximation of the number of elastic collisions occurring per inelastic collision. The value $-\ln(R)$ is the path length (in units of MFPs) traveled by the electron between collisions. Thus knowing the number of elastic collisions occurring and the path length traveled between collisions allows one to write (13) as the expression for the total path length s (in units of MFPs) traveled between inelastic collisions. The type of inelastic event is then calculated.

4. Sensitivity Study

The influence of the cross sections (both differential and total) on the spatial electron energy degradation process is the subject of this section. The elastic differential cross section affects the spatial aspects of electron degradation the most, and thus its effects will de discussed most thoroughly.

A Monte Carlo spatial energy deposition approach described in section 3 is used to degrade the electrons. In order to characterize the influence of the cross sections on the spatial energy deposition, the intensity profile of the 3914-Å emission will be used. This emission results from the excitation of the N_2^+ $B\,^2\Sigma_u^+$ state.

The 3914-Å emission is observed in aurorae and has been used by some experimenters [namely, *Grün*, 1957; *Cohn and Caledonia*, 1970; *Barrett and Hays*, 1976] to calculate a range for the electrons. This range is found by extrapolating the linear portion of the 3914-Å intensity plot to the z axis. An illustration of finding the ranges for two intensity plots from a Monte Carlo calculation is given in Figure 3.

The EX phase function is used as the elastic scattering phase function in all of the degradation calculations that follow,

unless otherwise specified. Before comparing the EX and the SR phase functions, first consider the influence of the inelastic differential cross sections.

The primary doubly differential cross section is substantially forward peaked [see *Porter et al.*, 1976]. Therefore, for comparison, it is assumed that no scattering of the primary electron was incurred during the ionization event. There was virtually no observed difference in the two 3914-Å intensity plots that resulted; thus the primary scattering in an ionization event is insignificant.

It is of interest to determine if the secondary doubly differential cross section affects the spatial energy deposition process. To do this, a comparison was made in a Monte Carlo calculation using, first, (6) and, second, an isotropic secondary scattering function. Again, no difference was discernable in the two resulting 3914-Å intensity plots.

A comparison was next made concerning the significance of the ad hoc inelastic excitation scattering assumed. If no scattering was allowed below 100 eV due to the inelastic excitation events, then the range was increased by about 7% for incident electrons of 0.3 and 0.1 keV. The incident electrons with energy 1.0 keV and above were not affected by this change.

The two elastic phase functions, EX and SR, were next compared at several incident electron energies between 0.1 and 5.0 keV. The ranges (given in grams per square centimeter) are presented in Table 4 from several sources including three experimental papers and one other theoretical calculation. The *Barrett and Hays* [1976] work is the most recent and may be the most accurate. The range of electron energies used was also about the same as that used in this work; thus we compare our Monte Carlo calculations with *Barrett and Hays* [1976].

The EX and SR range results bracket the range values from *Barrett and Hays* [1976] at the incident energies of 0.3, 1.0, 2.0, and 5.0 keV. If the experimental work is correct, then we can draw the conclusion that the SR phase function exhibits too much scatter while the EX phase function exhibits too little scatter.

A comparison of the two elastic phase functions with the experimental work of *Barrett and Hays* [1976] is given in Figure 3. This is a longitudinal intensity plot for an incident electron energy of 2 keV.

The intensity profiles can also be calculated in directions perpendicular to the z axis. These radial intensity profiles are calculated with the use of the EX phase function and are compared with both experimental and theoretical work in Figure 4. Both the ρ and the z values given in this figure are in units of fractions of the total range. The results from this work appear to agree better with the *Barrett and Hays* [1976] data than does the *Berger et al.* [1974] work. The *Berger et al.* [1974] data do agree better with the *Cohn and Caledonia* [1970] and with the *Grün* [1957] data. The difference in the results from this calculation and those of *Berger et al.* [1974] could be due to several reasons (three of which are mentioned here): (1) The Monte Carlo techniques are not the same; (2) the cross sections are not the same; and (3) the energy cutoffs are not the same. (In this work the primary, secondaries, and tertiaries are followed down to 2 eV, and in the work by *Berger et al.* [1974] the primary and secondaries are followed down to 200 eV.)

5. Spatial Yield Spectra

The work of *Green et al.* [1977] concentrated on the two-variable or nonspatial yield spectrum $U(E, E_0)$. The advantages of working with the yield spectrum were pointed out in that paper. One of the nice properties of $U(E, E_0)$ is its simple nature. It was hoped that the spatial yield spectra $U(E, z, E_0)$ and $U(E, \rho, z, E_0)$ hold the same simple properties.

TABLE 4. Range Data (in 10^{-6} gm/cm^2) at Several Energies E (in keV)

E, keV	EX	SR	BH	CC	G	BSM
0.1	0.37	0.34	(0.53)	(0.07)	(0.08)	···
0.3	1.25	0.95	1.06	(0.51)	(0.56)	···
1.0	6.45	5.57	5.72	(4.17)	(4.57)	···
2.0	18.6	16.8	17.7	14.0	(15.4)	15.2
5.0	91.5	75.9	83.0	69.7	76.4	71.9

The second column EX, third column SR, fourth column BH [*Barrett and Hays*, 1976], fifth column CC [*Cohn and Caledonia*, 1970], sixth column G [*Grün*, 1957], and seventh column BSM [*Berger et al.*, 1974] range values are presented. Numbers in parenthesis are those calculated from formulae given in those papers and thus were not actually measured by the experimenters.

The three-variable spatial yield spectrum is given by (in units of $[\text{eV}/(\text{gm/cm}^2)]^{-1}$)

$$U(E, z, E_0) = \frac{N(E, z)}{\Delta E\, \Delta z} \tag{14}$$

Here, $N(E, z)$ is the total number of electrons that existed in the spatial interval Δz centered at z and, also, in the energy interval ΔE centered at E after the incident electron and all its secondaries and tertiaries had been completely degraded in energy. This number $N(E, z)$ does not include the electrons in the rectangle that were elastically scattered. (There is no real interest here in the elastic events, and below 30 eV no elastic events are recorded anyway.)

The three-variable yield spectrum for an incident energy of 1 keV is presented in Figure 5 at three longitudinal distances. This $U(E, z, E_0)$, although more complex than the nonspatial $U(E, E_0)$, has some nice general characteristics that continue throughout the entire incident range (from 0.1 keV up to 5.0 keV). It is therefore reasonable to continue the philosophy of analytic representation pursued in *Green et al.* [1977]. The analytic properties of $U(E, z, E_0)$ will permit researchers to infer important spatially derived properties of N_2 with a degree

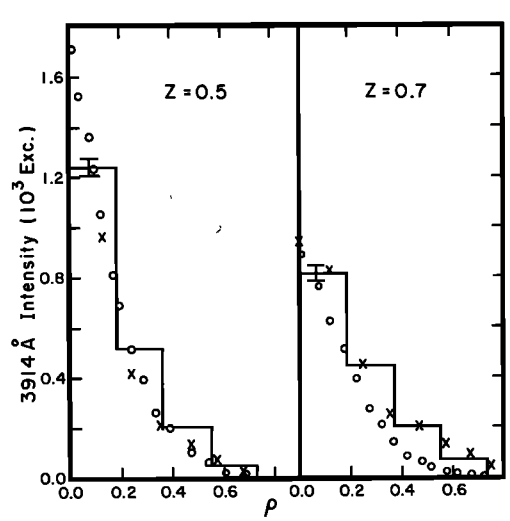

Fig. 4. Intensity plots for electrons with incident energy 5.0 keV are presented at two z values as functions of ρ. The solid line histogram indicates the results using EX. The crosses denote the experimental data of *Barrett and Hays* [1976], and the circles denote the theoretical work of *Berger et al.* [1970].

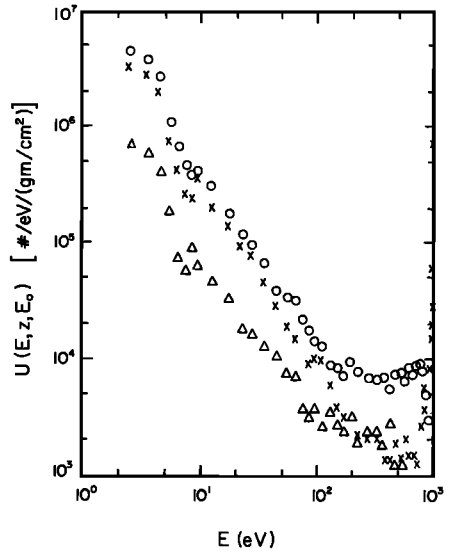

Fig. 5. Three-variable spatial yield spectrum for an incident energy of 1 keV given at three longitudinal distances (in fractions of the range): $z = 0.0739$, represented by crosses; $z = 0.429$, circles; and $z = 0.961$, triangles.

of accuracy useful in many atmospheric and laboratory applications.

It should be noted that at the small longitudinal distances a fairly large 'source' term persists at energies $E = E_0$. In the interval from about 4 eV to about 10 eV there is a noticeable dip (see Figure 5) in the yield spectra. In this range (see Figure 2), the total inelastic cross section also shows a very large dip. As a result of this small inelastic cross section between the energies of 4 and 10 eV, many of these low-energy electrons will travel out of the altitude region of interest before interacting inelastically with N_2.

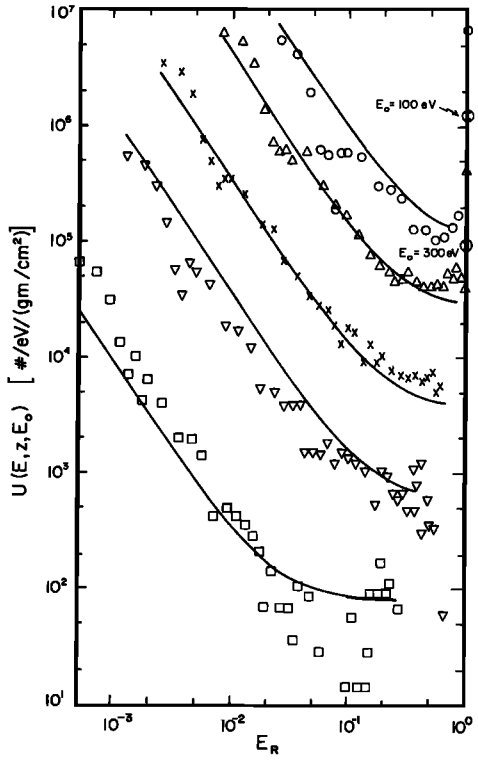

Fig. 6. Three-variable spatial yield spectrum $U(E, z, E_0)$ is plotted as a function of E_R. The Monte Carlo calculations are represented by symbols for each z (in fractions of the range) and E_0 (in keV): circles, $z = 0.126$, $E_0 = 0.1$; triangles, $z = 0.316$, $E_0 = 0.3$; crosses, $z = 0.606$, $E_0 = 1.0$; inverted triangles, $z = 0.928$, $E_0 = 2.0$; and squares, $z = 1.052$, $E_0 = 5.0$. The analytic fit using (15) is represented by the solid line with the source term contribution represented by a cross within a circle.

For the purposes of many applications it is useful to represent the yield spectra by

$$U'(E, z, E_0) = U_a'(E, z, E_0)\theta(E_0 - E - E_\theta) - \delta(E_0 - E)D(z, E_0) \quad (15)$$

(following the notation of *Green et al.* [1977]), where θ is the Heaviside function with E_θ the minimum threshold of the states considered, and $\delta(E_0 - E)$ is the Dirac delta function which allows for the contribution of the source itself. The $U_a(E, z, E_0)$ is represented approximately by

$$U_a'(E, z, E_0) = A(z, E_0) + B_1(z, E_0)[E_R]^{B_2} + C_1(z, E_0)[E_R]^{C_2} \quad (16)$$

where $E_R = E/E_0$ and the remaining parameters are defined in Appendix 2.

The yield of any state is then found from

$$J_j(z, E_0) = \int_{z-(\Delta z/2)}^{z+(\Delta z/2)} \int_{W_j}^{E_{ul}} U'(E, z, E_0)p_j(E)dE\,dz \quad (17)$$

where the upper limit of integration E_{ul} is given in Appendix 2 and $p_j(E)$ is the probability for excitation of the N_2 molecule to the jth state with a loss of excitation energy W_j by an incident electron of energy E. As the electrons penetrate further and further into the medium, they lose more and more of the high-energy particles. The energy E_{ul} is thus a cutoff energy which must be invoked.

Equation (15) represents the yield spectra data fairly well in

TABLE 5. Comparison Between the Yield of the 3914-Å Emission ((0.5 cm)$^{-1}$) From the MC Calculation (Column MC) and With the Use of (15) in (17) (Column AF) for Several Incident Energies E_0 and Longitudinal Distances z (in Fractions of the Range)

E_0, keV	z	MC	AF
0.1	0.01	280	287
0.1	0.2	240	272
0.1	0.5	155	168
0.1	0.8	70.0	82.3
0.1	1.0	35.2	49.7
0.3	0.01	452	406
0.3	0.2	626	523
0.3	0.5	490	429
0.3	0.8	174	177
0.3	1.0	74.2	73.2
1.0	0.01	550	556
1.0	0.2	740	797
1.0	0.4	860	908
1.0	0.7	500	456
1.0	1.0	100	91.9
2.0	0.01	600	578
2.0	0.2	780	841
2.0	0.4	1050	995
2.0	0.7	600	517
2.0	1.0	130	85.5
5.0	0.01	1330	1323
5.0	0.2	1760	1927
5.0	0.4	2100	2337
5.0	0.7	1380	1214
5.0	1.0	200	160

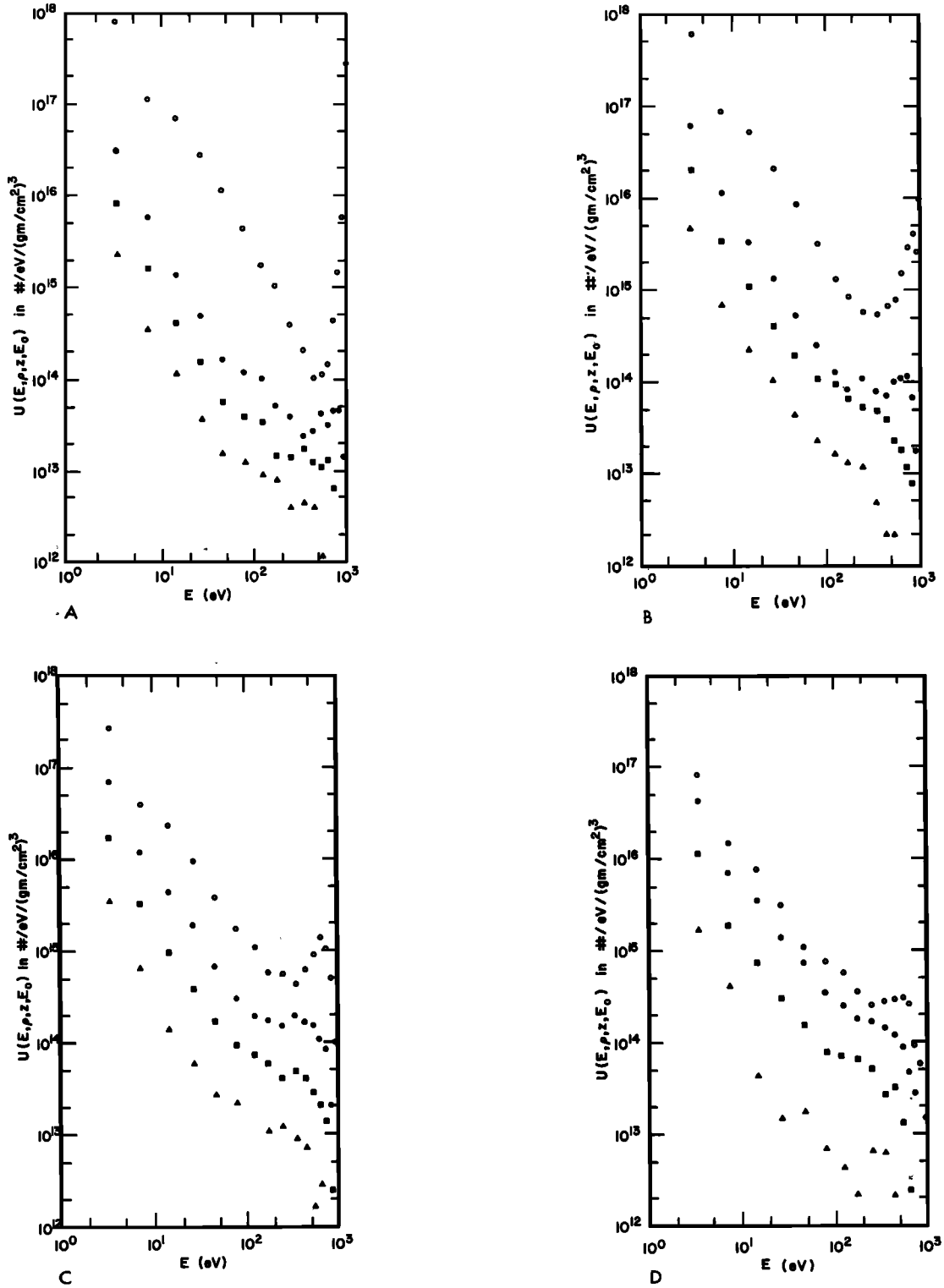

Fig. 7. Four-variable spatial yield spectra for an incident electron energy of 1 keV given at four longitudinal distances: (*a*) $z = 0.061$, (*b*) $z = 0.305$, (*c*) $z = 0.549$, and (*d*) $z = 0.793$. At each longitudinal cut the yield spectrum is given at four radial distances: open circles represent $\rho = 0.061$; filled circles, $\rho = 0.305$; squares, $\rho = 0.549$; and triangles, $\rho = 0.793$.

this regime of incident electron energies. The fit can be seen in Figure 6 for five incident energies at five longitudinal values.

A comparison is given in Table 5 between the yield using (17) and the yield using the Monte Carlo calculation for several incident energies and longitudinal values for the yield of the 3914-Å emission. The two calculations are in fair agreement throughout the entire range considered. It should be noted, however, that (15) is not accurate at longitudinal values in the backscatter direction.

One check on the three-variable analytic yield spectrum $U'(E, z, E_0)$ is to compare the $U_I(E, E_0)$ found from

$$U_I(E, E_0) = \int_0^\infty U'(E, z, E_0)\, dz \qquad (18)$$

with the $U(E, E_0)$ calculated by *Green et al.* [1977]. The two functions are amazingly close except for a slight deviation at the higher values of $E_0(E_0 > 0.5$ keV) and $E(E > 0.8E_0)$. The $U_f(E, E_0)$ is lower than the $U(E, E_0)$ from *Green et al.* [1977] in those energy regions. One would expect the $U_f(E, E_0)$ to be slightly less than the $U(E, E_0)$, since the backscattered particles are not included in the $U_f(E, E_0)$. Since the $U_f(E, E_0)$ exhibits the behavior described above, the $U'(E, z, E_0)$ therefore slightly overestimates the lower-energy ($E < 0.5E_0$) yield spectra.

Consider now the use of an analytic spatial yield spectrum with an incident electron energy flux of $\phi(E_0)$ (in units of el/cm² s eV). A yield $J_j[z, \phi(E_0)]$ (in units of excitations/cm³ s) of the jth state with a threshold W_j can be calculated using

$$J_j[z, \phi(E_0)] = \int_{W_j}^{\infty} \int_{W_j}^{E_{ul}} \phi(E_0)U'(E, z, E_0) \cdot \rho(z)p_f(E)\, dE\, dE_0 \quad (19)$$

where $\rho(z)$ is the density (in grams per cubic centimeter) of the N_2 gas at altitude z.

The four-variable spatial yield spectrum $U(E, \rho, z, E_0)$ can be calculated from the Monte Carlo deposition program in a manner similar to the way that the $U(E, z, E_0)$ was calculated. Here (in units of particles/eV (gm/cm²)³),

$$U(E, \rho, z, E_0) = \frac{N(E, \rho, z)}{\pi[(\rho + (\Delta\rho/2))^2 - (\rho - (\Delta\rho/2))^2]\Delta E\, \Delta z} \quad (20)$$

where $N(E, \rho, z)$ is the total number of inelastic collisions that existed in the cylindrically symmetric ring-shaped volume with length Δz and thickness $\Delta\rho$ centered on (ρ, z) and, also, in the energy interval ΔE centered at E. This $N(E, \rho, z)$ includes inelastic collisions of the incident electrons and all its secondaries and teriaries after they have been completely degraded in energy.

The four-variable spatial yield spectrum is presented in Figures 7 *a–d* for an incident electron energy of 1 keV. It is given at four radial distances at each longitudinal cut (all in units of fractions of the range). The $U(E, \rho, z, E_0)$ from other incident electron energies are not presented here but show a similar type of behavior.

The shape of $U(E, \rho, z, E_0)$ is observed to be quite similar to $U(E, z, E_0)$ (see Figures 5 and 6) and, indeed, even to $U(E, E_0)$ [see *Green et al.*, 1977, Figure 1*e*]. The lower energy power fall-off is $\propto E^{-1.6}$ in all three yield spectra. All three spectra also exhibit a constant component in the middle energies with the source term feature at the incident energy ($E_R = 1.0$).

The four-variable and three-variable spatial yield spectra illustrate a tendency to increase at higher values of energy ($E_R \approx 0.9$–1.0) and at the lower values of z and ρ. This feature is not as prominent in the nonspatial yield spectrum $U(E, E_0)$, which is calculated by integrating over the spatial component of the spatial yield spectra. In the integration process the higher-energy spectra increase is averaged out by the equally important higher-energy spectra decrease exhibited at the higher values of z and ρ.

6. Conclusions

A Monte Carlo method of energy degradation has been used in this work to spatially deposit the energy of incident electrons with energies from 0.1 to 5.0 keV. This stochastic degradation method deposited energy in a collision-by-collision process down to 30 eV, and a multiple elastic scattering distribution was used from 30 eV down to the cutoff energy of 2 eV. Recently published primary and new secondary differential ionization cross section forms have been used. The scattering of the primary is in inelastic collisions minuscule when compared to the elastic event scattering, and the form for secondary scattering has no effect on the final degradation process (seen also in the work by *Strickland et al.* [1976]).

Two forms were used for elastic scattering: (1) the screened Rutherford form and (2) a form which contains an exponential fall-off at the low angles and backscatter at energies less than 200 eV. Electrons degraded with the use of the second form exhibited the further penetration at all incident energies used. The longitudinal 3914-Å intensity plots that resulted from the two forms bracketed the experimental results of *Barrett and Hays* [1976]. The radial 3914-Å intensity plots calculated with the use of the second form were fairly close to these experimental results (when ρ and z were normalized to the unit of fraction of the range).

Because of this reasonable agreement, a solution to the equation of transfer can be given in terms of the three-variable ($U(E, z, E_0)$) and four-variable ($U(E, \rho, z, E_0)$) spatial yield spectra. These spectra exhibit fairly simple characteristics which, if analytically represented, could be applied conveniently to the calculation of a yield at any position in the medium. The $U(E, z, E_0)$ was, in fact, analytically represented with the use of (15), and work is now being carried out on the $U(E, \rho, z, E_0)$ to define and characterize its major attributes.

Appendix 1: Analytic Expressions Used in (6) and (7)

$$B(E) = 0.0448 + \left(\frac{E}{72900\text{ eV}}\right)^{0.91}$$

$$C(T) = \frac{36.6\text{ eV}}{T + 183\text{ eV}}$$

$$\theta_0(E, T) = 0.873 + \frac{\theta_A(E)}{T + \theta_B(E)}$$

$$\theta_A(E) = 20\text{ eV} + 0.042E$$

$$\theta_B(E) = 28\text{ eV} + 0.066E$$

$$N_f(E, T) = \frac{-2\pi C}{B^{1/2}}\left\{\tan^{-1}\left[\frac{-B^{1/2}(1 + \cos\theta_0)}{C}\right] - \tan^{-1}\left[\frac{B^{1/2}(1 - \cos\theta_0)}{C}\right]\right\}$$

$$A(E) = \sigma_0 \frac{5.30}{E} \ln\left[\frac{E}{1.74\text{ eV}}\right]$$

$$T_0(E) = 4.71\text{ eV} - \frac{1000\text{ (eV)}^2}{E + 31.2\text{ eV}}$$

$$\Gamma(E) = 13.8\text{ eV}\, E/(E + 15.6\text{ eV})$$

$$\sigma_0 = 1 \times 10^{-16}\text{ cm}^2$$

Appendix 2: Parameter Expressions and Values for Use in (15)

$$A(z, E_0) = \frac{a_1(E_0)}{[z_R - a_2(E_0)]^2 + a_3(E_0)}$$

$$B_1(z, E_0) = \frac{b_{11}(z, E_0)}{[z_R - b_{12}(E_0)]^2 + b_{13}}$$

$$C_1(z, E_0) = \frac{c_{11}(z, E_0)}{e^{z_R/c_{12}} + 1}$$

$$D(z, E_0) = \frac{d_1(E_0)}{e^{z_R/d_2} + 1}$$

$$a_1(E_0) = a_{11}\xi_0^{a_{12}}$$

$$a_2(E_0) = a_{21}\left(1 - \frac{a_{22}}{\xi_0}\right)$$

$$a_3(E_0) = a_{31} + \frac{a_{32}}{\xi_0}$$

$$b_{11}(z, E_0) = \frac{b_{111}\xi_0^{b_{112}}\left[1 + \dfrac{(1 - \xi_0)}{b_{113}}\right]}{[\exp\{[z_R - f_1(E_0)]/f_2(E_0)\} + 1]}$$

$$b_{12}(E_0) = b_{121}\left(1 - \frac{b_{122}}{\xi_0}\right)$$

$$c_{11}(z, E_0) = c_{111}\,\xi_0^{c_{112}}/[\exp\{[z_R - f_1(E_0)]/f_2(E_0)\} + 1]$$

$$d_1(E_0) = d_{11}\,\xi_0^{d_{12}}$$

$$f_1(E_0) = f_{11}\left(1 + \frac{f_{12}}{\xi_0}\right)$$

$$f_2(E_0) = f_{21}\,\xi_0^{f_{22}}$$

$$R_g(E_0) = r_1 + r_2\,\xi_0^{r_3} \text{ (range of an electron of primary energy } E_0)$$

$$E_{ut} = \frac{E_0}{[e^{(z_R - g_1(E_0))/g_2} + 1]}$$

$$g_1(E_0) = g_{11}\left(1 + \frac{g_{12}}{\xi_0}\right)^{-1}$$

$$\xi_0 = \frac{E_0 \text{ (in eV)}}{1000 \text{ eV}}$$

$$z_R = \frac{z}{R_g(E_0)}$$

TABLE A1. Parameter Expressions and Values for Use in (15)

Parameter	Value	Parameter	Value
a_{11}	587	d_{11}	0.6×10^6
a_{12}	−1.63	d_{12}	−1.68
a_{21}	0.4	d_2	0.2
a_{22}	0.075	f_{11}	0.9
a_{31}	0.1	f_{12}	0.044
a_{32}	0.019	f_{21}	0.104
b_{111}	81	f_{22}	−0.39
b_{112}	−1.8	g_{11}	0.85
b_{113}	8.0	g_{12}	0.07
b_{121}	0.4	g_2	0.2
b_{122}	0.05	r_1	2.27×10^{-7} gm/cm^2
b_{13}	0.2	r_2	6.22×10^{-6} gm/cm^2
B_2	−1.52	r_3	1.67
c_{111}	1.30×10^4		
c_{112}	−1.5		
c_{12}	0.15		
C_2	10		

Acknowledgments. This research was supported by the Planetary Atmospheres program of the National Aeronautics and Space Administration under grant NGL-10-005-008. The authors would also like to thank the referees (S. M. Seltzer and an anonymous referee) for their helpful criticisms and comments about this paper.

The Editor thanks S. M. Seltzer and W. E. Swartz for their assistance in evaluating this paper.

REFERENCES

Banks, P. M., C. R. Chappell, and A. F. Nagy, A new model for the interaction of auroral electrons with the atmospheres: Spectral degradation, backscatter, optical emission, and ionization. *J. Geophys. Res., 79,* 1459, 1974.

Barrett, J. L., and P. B. Hays, Spatial distribution of energy deposited in nitrogen by electrons, *J. Chem. Phys., 64,* 743, 1976.

Berger, M. J., S. M. Seltzer, and K. Maeda, Energy deposition by auroral electrons in the atmosphere, *J. Atmos. Terr. Phys., 32,* 1015, 1970.

Berger, M. J., S. M. Seltzer, and K. Maeda, Some new results on electron transport in the atmosphere, *J. Atmos. Terr. Phys., 36,* 591, 1974.

Blaauw, H. J., F. J. de Heer, R. W. Wagenaar, and D. H. Barends, Total cross sections for electron scattering from N_2 and He, *J. Phys. B, 10,* L299, 1977.

Cartwright, D. C., A. Chutjian, S. Trajmar, and W. Williams, Electron impact excitation of the electronic states of N_2, I, Differential cross sections at incident energies from 10 to 50 eV, *Phys. Rev. A, 16,* 1013, 1977.

Chutjian, A., D. C. Cartwright, and S. Trajmar, Electron impact excitation of the electronic states of N_2, III, Transitions in the 12.5–14.2 eV energy-loss region at incident energies of 40 and 60 eV, *Phys. Rev. A, 16,* 1052, 1977.

Cicerone, R. J., and S. A. Bowhill, Photoelectron escape fluxes obtained by a Monte Carlo technique, *Radio Sci., 5,* 49, 1970.

Cicerone, R. J., and S. A. Bowhill, Photoelectron fluxes in the ionosphere computed by a Monte Carlo method, *J. Geophys. Res., 76,* 8299, 1971.

Cohn, A., and G. Caledonia, Spatial distribution of the fluorescent radiation emission caused by an electron beam, *J. Appl. Phys., 41,* 3767, 1970.

Green, A. E. S., and T. Sawada, Ionization cross sections and secondary electron distributions, *J. Atmos. Terr. Phys., 34,* 1719, 1972.

Green, A. E. S., C. H. Jackman, and R. H. Garvey, Electron impact on atmospheric gases, 2, Yield spectra, *J. Geophys. Res., 82,* 5104, 1977.

Grün, A. E., Lumineszenz-photometrische Messungen der Energieabsorption in Strahlungsfeld von Elektronenquellen eindimensionaler Fall in Luft, *Z. Naturforsch., 12a,* 89, 1957.

Heaps, M. G., and A. E. S. Green, Monte Carlo approach to the spatial deposition of energy by electrons in molecular hydrogen, *J. Appl. Phys., 45,* 3183, 1974.

Herrmann, D., K. Jost, and J. Kessler, Differential cross sections for elastic electron scattering, II, Charge cloud polarization in N_2, *J. Chem. Phys., 64,* 1, 1976.

Ivanov, V. Ye., N. K. Osipov, and V. A. Shneyder, Analytic representation of the elastic scattering cross sections of low-energy electrons by atmospheric gases, *Geomagn. Aeron., 17,* 165, 1977.

Jackman, C. H., Spatial and energetic aspects of electron energy deposition, Ph.D. thesis, Univ. of Fla., Gainesville, 1978.

Jackman, C. H., R. H. Garvey, and A. E. S. Green, Electron impact on atmospheric gases, 1, Updated cross sections, *J. Geophys. Res., 82,* 5081, 1977.

Jasperse, J. R., Boltzmann-Fokker-Planck model for the electron distribution function in the earth's ionosphere, *Planet. Space Sci., 24,* 33, 1976.

Jasperse, J. R., Electron distribution function and ion concentrations in the earth's lower ionosphere from Boltzmann-Fokker-Planck theory, *Planet. Space Sci., 25,* 743, 1977.

Jung, K., E. Schubert, D. A. L. Paul, and H. Ehrhardt, Angular correlation of outgoing electrons following ionization of H_2 and N_2 by electron impact, *J. Phys. B, 8,* 1330, 1975.

Kutcher, G. J., and A. E. S. Green, Multiple elastic scattering of slow electrons: Parametric study for H_2, *J. Appl. Phys., 47,* 2175, 1976.

Mantas, G. P., Theory of photoelectron thermalization and transport in the ionosphere, *Planet. Space Sci., 23,* 337, 1975.

Moliere, G., Theory of scattering of fast charged particles. I, Single scattering in a screened Coulomb field, *Z. Naturforsch., 2a,* 133, 1947.

Moliere, G., Theory of scattering of fast charged particles, II, Plural and multiple scattering, *Z. Naturforsch., 3a,* 78, 1948.

Opal, C. B., E. C. Beaty, and W. K. Peterson, Tables of secondary-electron-production cross sections, *Atomic Data, 4,* 209, 1972.

Porter, H. S., and F. W. Jump, Jr., Analytic total and angular elastic electron impact cross sections for planetary atmospheres, *Tech. Rep. CSC/TM-78/CO17,* prepared for Goddard Space Flight Center by Computer Sci. Corp., Greenbelt, Md., 1978.

Porter, H. S., C. H. Jackman, and A. E. S. Green, Efficiencies for production of atomic nitrogen and oxygen by relativistic proton impact in air, *J. Chem. Phys., 65,* 154, 1976.

Shyn, T. W., R. S. Stolarski, and G. R. Carignan, Angular distribution of electrons elastically scattered from N_2, *Phys. Rev. A, 6,* 1002, 1972.

Strickland, D. J., D. L. Book, T. P. Coffey, and J. A. Fedder, Transport equation techniques for the deposition of auroral electrons, *J. Geophys. Res., 81,* 2755, 1976.

Walt, M., W. M. MacDonald, and W. E. Francis, Penetration of auroral electrons into the atmosphere, *Physics of the Magnetosphere,* p. 534, edited by R. L. Carovillano, J. F. McClays, and H. R. Radoski, D. Reidel, Hingham, Mass., 1967.

(Received October 26, 1978;
revised January 17, 1979;
accepted January 17, 1979.)